Multi-Domain Electric Drivetrain Modeling for UAM-Scale eVTOL Aircraft

Meaghan Podlaski Graduate Student
Robert Niemiec Research Scientist
Luigi Vanfretti Associate Professor
Farhan Gandhi MOVE Director

ABSTRACT

This paper presents the modeling and validation of an electric drivetrain through an object-oriented, equation-based framework that includes aerodynamics, electric machine, power electronic converter and battery models at various levels of detail. The proposed drivetrain model considers different losses in the machine and levels of fidelity for the power source and converters. It is simulated with various maneuvers, aiming to show the effects of modeling simplifications on the behavior of UAMs. These studies show that the level of detail in the motors and power system has significant impact on the dynamic response and power consumption of the system. This is most evident in the cases where the system uses a detailed battery model and in the cases where the switching electrical components are used, creating a torque ripple.

NOTATION

b	Motor friction constant
EMF	Electromotive force
i	Motor current
I	Motor effective inertia
i_{np}	Battery cell current for the nth cell in series and pth cell in parallel
K_e	Motor transformation coefficient
L	Motor inductance
OCV	Open circuit voltage
OCV_{np}	Battery open circuit voltage for the nth cell in series and pth cell in parallel
R	Motor resistance
$P_{loss,d}$	Frictional loss in the motor
PWM	Pulse width modulation
Q_{aero}	Moment of the aerodynamic torque
Q_{motor}	Moment of the motor
SoC	State of charge
V_a	Voltage applied to the motor
$V_{battery}$	Battery cell voltage for the nth cell in series and pth cell in parallel
X	Motor impedance
$Z_{battery}$	Battery impedance for the nth cell in series and pth cell in parallel
Ω	Motor speed
Ω_{out}	Motor speed
Ω_{ref}	Reference motor speed
τ	Torque generated by the motor
τ_a	Time constant for the motor impedance
τ_d	Torque applied to the damper in the motor
τ_{out}	Torque applied to the rotor model from the motor
τ_{rotor}	Torque produced by the rotor model

Presented at at the VFS International 77th Annual Forum & Technology Display, May 10–14, 2021.

INTRODUCTION

Distributed electric propulsion has enabled a vast array of new concept vehicles, largely centered around NASA's Advanced Air Mobility (AAM) initiative (Ref. 1) and Uber Elevate (Ref. 2). Most of these concepts take advantage of the ability of electric motors to operate at a relatively wide range of RPM compared to conventional turbine-driven drivetrains, which have a narrow band of efficient operating speeds.

Within the VTOL community, substantial attention has been paid to the effectiveness of variable-RPM rotor systems on Urban Air Mobility, a subset of AAM, focused on passenger transport operations. Variable-RPM rotor systems were compared to variable-pitch systems at NASA Ames Research Center (Refs. 3,4), and at the Center for Mobility with Vertical Lift (MOVE, Ref. 5). Both of these studies examined variants of the quadcopter concept put forward in (Ref. 6), finding that variable-RPM systems were not viable unless drivetrain limits were significantly higher than current design trends suggest. In Ref. 5, it was found that these same limitations were applicable to variable-pitch systems, due to the large motor torque required to meet yaw handling qualities specifications.

Also at MOVE, recent work (Ref. 7) explored the impact of motor dynamics on the handling qualities of single-passenger vehicles with different numbers of rotors at a fixed gross weight and disk loading, and related research (Ref. 8) explored the same on quadcopters at different AAM-relevant scales. Both studies generally found that having smaller rotors, whether by possessing more, smaller rotors or operating at a lower gross weight, reduced the over-sizing necessary for the motors to handle current commands during maneuvers.

All of the above studies utilized an idealized motor model, using simplified DC motor equations to capture motor dynamics, treating the armature voltage as a command. However, electrical machine dynamics are much more complex than the behavior described by such equations (Refs. 9, 10). In addition, the ideal DC motor model neglects the effects of the electronic speed controller (Ref. 11), which provides the

commands to change the voltage and/or current to different parts of the stator (the stationary component of a brushless DC motor), called "phases." The rapid switching of voltage and/or current required to track a desired speed is carried out by a DC/DC power electronic converter (Ref. 10). Such converters have different internal switch configurations (known as topologies, (Ref. 12) and control modes (Refs. 11, 13), e.g. armature voltage control or field-oriented control, (Ref. 14), which result in switching losses at the converter itself. Moreover, the switching also introduces a distortion known as voltage/current ripple to the motor terminals. While filters formed by passive components (capacitors and inductors) can be designed to minimize the ripple, it is impossible to completely remove it (Refs. 14,15). Regardless of its magnitude, the voltage/current ripple will affect the desired performance of the motor and lead to different types of losses in the machine, most of which will ultimately impact the thermal management needs (Ref. 16) and result in torque ripple that may lead to unacceptable speed ripple, vibration, and acoustic noise (Ref. 17), all of which reduce the handling qualities and lifetime of the drivetrain. All of these aspects are impossible to capture using the simplified DC motor equations.

Previous studies have also assumed that the battery is a constant voltage source, without regard to aging, or power drain over the course of a flight. Naturally, as batteries discharge over the course of a flight, the pack voltage will drop, increasing the strain on the system (as voltage drops, current has to be increased to deliver the same amount of power), demanding additional effort from the DC/DC converter to deliver the required voltage/current and possibly leading to inadequate handling qualities or even a loss of control.

More sophisticated motor and battery models have been implemented on eVTOLs (Refs. 18–20), though these studies primarily examine performance metrics such as efficiency. However, higher-fidelity drivetrain models are needed for other design aspects such as thermal management (Refs. 16, 21), response and mitigation to failures (Refs. 21, 22), impact on aircraft handling (Refs. 17, 23), etc. For example, the importance of high-fidelity drivetrain modeling can be understood from results in Ref. 24, where a switched inverter model is connected to a battery and motor in a quadcopter. Large voltage and current ripples were created by transistor switching in the converter, which impacted system operation depending on the converter topology (Ref. 12), control (Ref. 13), etc. Higher-fidelity models would therefore allow for more realistic analyses, providing a broader insight to the experiments such as those in (Refs. 18–20), and to integrate electrical powertrains with other subsystems that depend on their performance, i.e. aerodynamic and thermal.

The objectives of the present study are:

- Application of multi-engineering domain (mechanical-electrical) models for an electric drivetrain with varying degrees of complexity, including detailed battery, machine, and power electronic converter models.
- Modeling drivetrain response for power source models, including an ideal power source, fully charged battery, and battery at 30% charge.
- Comparing drivetrain response for different machine configurations under various speed commands, namely quadcopters with fully-distributed batteries (where each motor has a dedicated power source) and a fully-centralized battery (where all rotors share a single power source).

Paper Organization

First, the drivetrain model is introduced and outlined. All of the components and variants of those components are explained.

In the next section, a second order speed command is applied to the drivetrain models to study their aerodynamic response and electrical dynamics.

Next, the brushless averaged DC motor is put into a quadrotor configuration. A heave, pitch, and roll maneuver is applied to the system using an ideal power source, fully charged battery, and battery at 30% charge. This allows us to study the impact of the battery's state of charge on the system performance.

Finally, a comparison of two battery layouts is presented. Specifically, a fully-distributed battery system versus a fully-centralized battery on a 300 lb quadcopter (that used in Ref. 8).

MODELING

Platform Description

The vehicle considered in this study is a 300lb quadcopter used in Ref. 8. The properties of this quadcopter and its rotors are listed in Table 1. The rotors are assumed to be linearly twisted and tapered and have a 10% R tip clearance. The motor parameters are based on the Hacker Q150-45-4 (Ref. 25), and are also included in Table 1.

The drivetrain consists of four main components: a controller, pulse width modulation (PWM) of the converter, a DC/DC converter, and a brushless DC machine as shown in Figure 1. Starting from the left-hand side of Fig. 1, a pulse-width modulated signal, which defines the instantaneous desired speed of the motor (based on vehicle-level control needs) is provided to a speed controller, which, among other things, regulates the voltage/current to track the desired speed. The controller feeds a signal to a power converter, which steps-up the voltag and commutates the battery voltage to a suitable waveform for the motor to meet the desired speed. The motor itself converts the electrical current to a mechanical torque, which drives the rotor at Ω_{out}.

Each component of the drivetrain is modeled at multiple levels of fidelity using Dassault Systèmes' Dymola software, which utilizes the equation-based modeling language, Modelica (Ref. 26), and contains several libraries for drivetrain modeling, including the *Brushless DC Drive* library (Ref. 27), and the *Battery* library (Ref. 28).

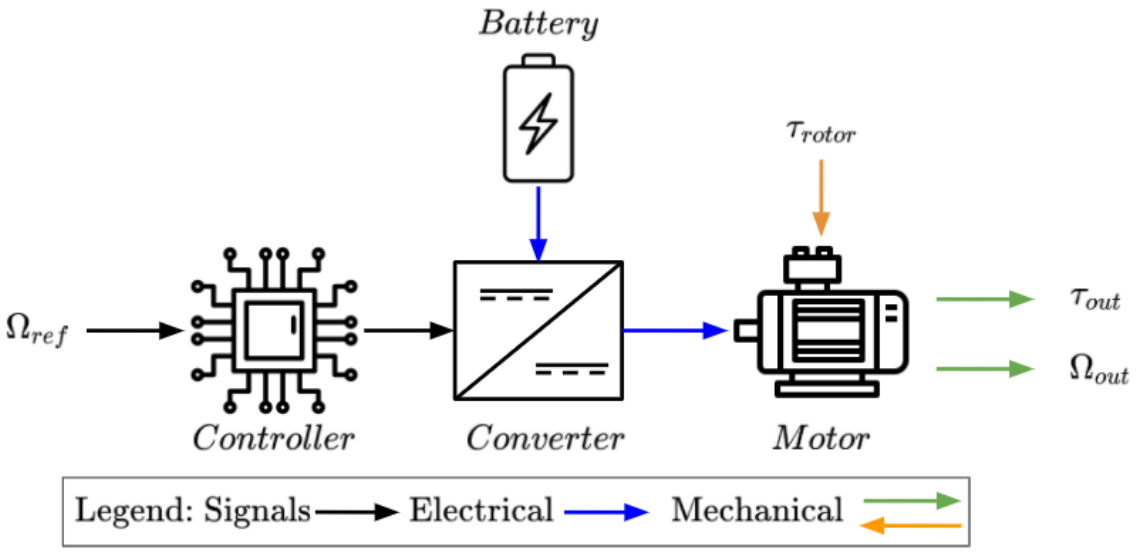

Figure 1: Electric powertrain schematic

Table 1: Aircraft Parameters

Vehicle Parameters	
Boom Length (m)	0.905
Gross Weight (kg)	136
I_{xx} (kg m^2)	43
I_{yy} (kg m^2)	51
I_{zz} (kg m^2)	84
Rotor Parameters	
Rotor Radius (m)	0.6096
Rotor Inertia (kg m^2)	0.063
Root Pitch (deg)	21.5
Linear Twist (deg)	-10.4
Solidity	0.09
Taper Ratio	2.5
Motor Parameters	
$K_e(Nm/A)$	0.1342
R (Ohm)	0.0155
L (μH)	4
b (Nms/rad)	3.71e-4

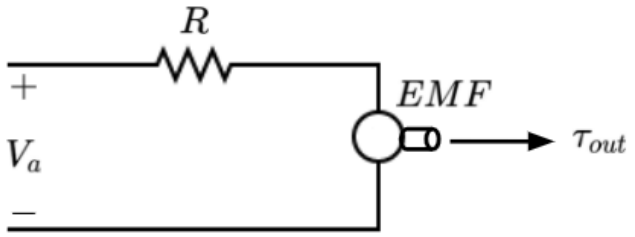

Figure 2: Circuit diagram of DC motor without inductance.

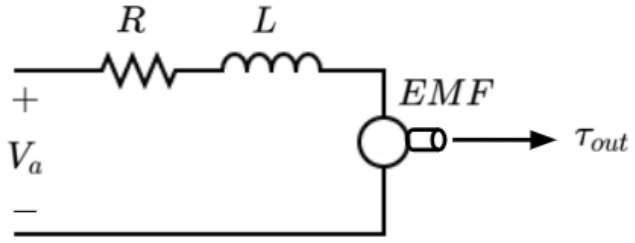

Figure 3: Circuit diagram of DC motor with inductance.

Motor models

In Figure 1, the motor can be modeled at multiple levels of fidelity to include different levels of losses. Four different models are used:

1. Simple DC motor without inductance
2. Simple DC motor with inductance
3. Brushless motor with averaged back EMF
4. Brushless motor with trapezoidal back EMF

Simple DC motor without inductance: The simplest representation of the motor is shown in Figure 2. The motor speed is governed by Eq. 1, where I represents the effective inertia (including the rotor blades), and the right-hand side is the net moment. The motor torque is proportional to the current, and the current is quasi-steady, given by Eq. 3.

$$I\frac{d\Omega}{dt} = Q_{\text{motor}} - Q_{\text{aero}} \tag{1}$$

$$Q_{\text{motor}} = K_e i \tag{2}$$

$$i = \frac{V - K_e\Omega}{R} \tag{3}$$

Simple DC motor with inductance: An inductance is added to the motor model in Figure 3. Due to the presence of the machine's inductance, the current no longer evolves instantaneously, but is governed by the dynamic equation, Eq. 4.

Otherwise, this model is identical to the previous.

$$L\frac{di}{dt} = V - Ri - K_e\Omega \tag{4}$$

By adding an inductance to the motor, a new time constant (τ_a) is added to the system. This time constant derivation is shown in Equation 5, where L is the motor inductance and R is the motor resistance. In many machines, the inductance is so small that the time constant does not have much impact on the system from the mechanical point of view, but whose electrical dynamics cannot be neglected when studying the electrical power train itself. For the Hacker Q150-45 brushless machine used in this study, the motor has a resistance of 0.0155 Ohm (Ref. 25) and inductance of 4μH (based on regression in Ref. 4). This results in a time constant of 258.06μs, or a settling time of 1ms. These time contants will interact with the power electronic converter and it's controls.

$$\tau_a = \frac{L}{R} \tag{5}$$

Brushless DC motor with averaged EMF: The brushless DC motor with averaged EMF considers builds off the simple motor models to include frictional losses in the machine. The motor model is shown in Figure 4. Equation 1 is modified to include a viscous torque, resulting in Eq. 6, where b is the effective damping due to viscosity in the air gap between the stator and rotor. Motor torque and current are governed by Eqs. 2 and 4, respectively. For the Hacker Q150-45, $b = 3.71e-4$.

$$I\frac{d\Omega}{dt} = Q_{\text{motor}} - Q_{\text{aero}} - b\Omega \tag{6}$$

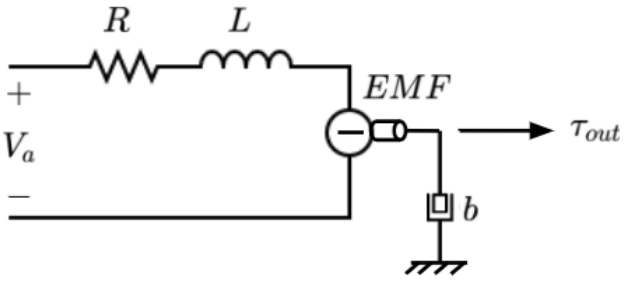

Figure 4: Circuit diagram of the averaged brushless motor.

Brushless DC motor with trapezoidal EMF: The brushless DC motor further increases complexity, as the motor's back EMF is component is replaced with a three-phase trapezoidal back EMF. Previously, the back EMF is a function of speed only; in this model, the back-EMF in each phase is also dependent on the motor position, as shown in Figure 5. The waveform is trapezoidal, therefore, this motor will be referred to as the "Trapezoidal DC motor" throughout this study. The resistance and inductance in each phase is half that of the whole motor. In a three phase motor, two phases are always

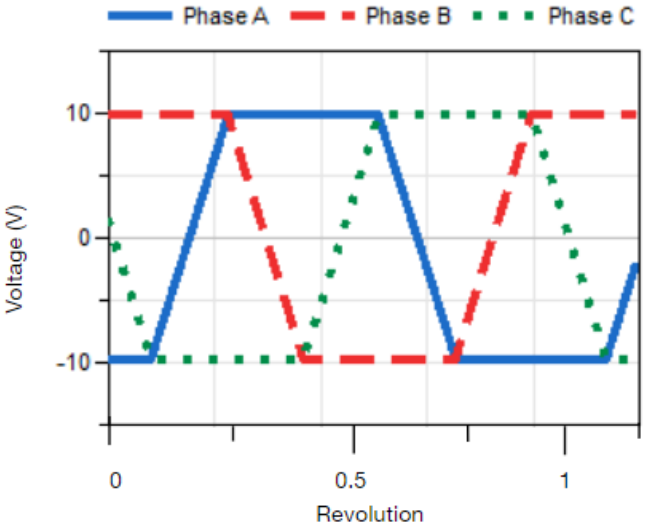

Figure 5: Back EMF of trapezoidal brushless machine with a duty cycle of 0.33.

conducting in series, so the impedance of each phase is added together as they are electrically in series with each other.

Since the trapezoidal motor configuration operates in three-phases, the converter and controller models include switching instead of the averaged conversion used in the previous models. The converter used with the trapezoidal motor shown in Figure 6 is a by a 3-phase full-bridge inverter that of diodes and transistors (represented as switches), that supplies the motor it they can produce the time-varying back EMF. Finally, the battery voltage needs to be stepped up before converted by the full-bridge inverter, this is done using an ideal buck-boost converter. Note that this converter is not shown in Fig. 6, but is a very commonly used converter (Ref. 14).

The PWM signal applied to the motor's converter is controlled using a six-step controller. Each pulse is separated by 60 degrees electrically to produce three sinusoidal voltages to apply to the machine. In Figure 6, the PWM signals are labelled such that there is a signal to control each diode in the converter for each phase, resulting in six signals.

Battery models

eVTOL systems are commonly modeled with ideal battery sources. Ideal battery sources can deliver any amount of current while maintaining a constant voltage. However, real-world batteries lose voltage when higher current is drawn (resistive losses and changes in battery chemistry), and as charge is depleted. These effects can be modeled using atable-based open circuit voltage (OCV) battery. The OCV battery schematic is shown in Figure 7, where each cell of the battery is modeled as an ideal voltage source, plus resistors and capacitors. The values of the capacitances and resistances are functions of the current draw, temperature, and state of charge of the battery, and are based on lookup-tables derived from experimental data on the Sanyo 18650 Li-Ion cylindrical cell (Ref. 28). To scale the battery voltage, n cells are wired

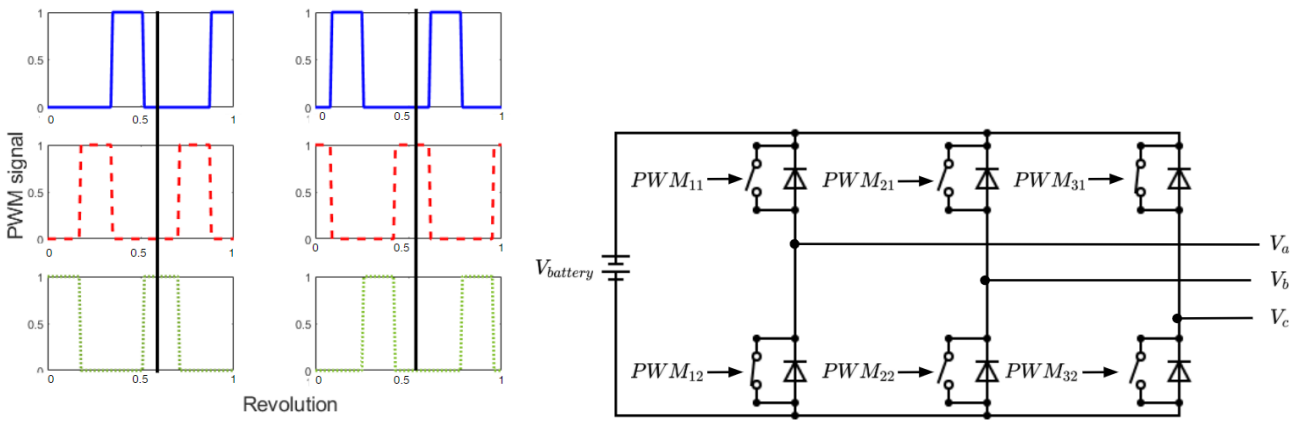

Figure 6: Switched three-phase converter with averaged input voltage

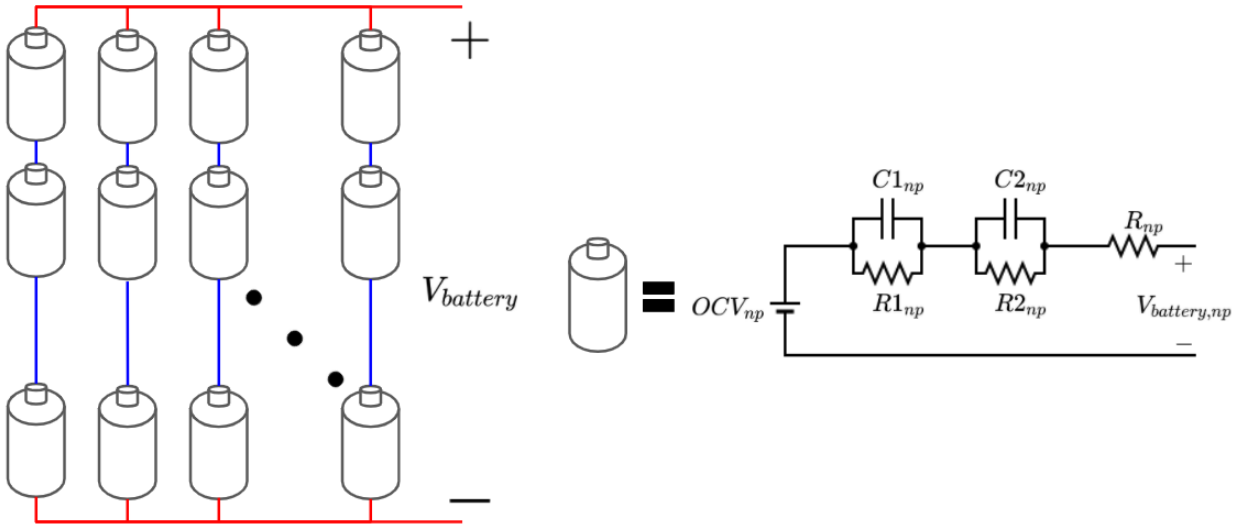

Figure 7: Battery schematic.

in series, and to scale the capacity, p sets of n cells are wired in parallel to produce a model for the battery pack.

The battery is modeled as matrix of parallel (p) and series (n) cells, as shown in Figure 7. Each individual cell produces a voltage using Equation 7. The impedance in each cell can be determined using Eq. 8.

$$V_{battery,ij} = OCV_{ij} - Z_{battery,ij} i_{ij} \tag{7}$$

$$Z_{battery,ij} = (R1_{ij} || C1_{ij}) + (R2_{ij} || C2_{ij}) + R_{ij} \tag{8}$$

MULTI-DOMAIN MODEL COUPLING IN SIMULINK

The drivetrain is modeled in its entirety using Modelica and is exported to interact with RMAC in MATLAB/Simulink as a Functional Mock-up Unit (FMU). An FMU contains a dynamic model that has been exported according to the Functional Mock-up Interface (FMI) standard, which allows for

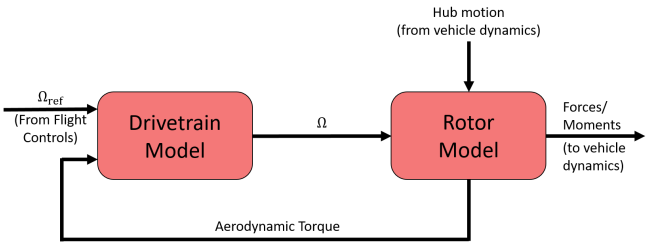

Figure 8: Integration of the drivetrain model with RMAC rotor model.

model export and/or co-simulation in many different simulation tools (Ref. 29). The inputs and outputs of the FMU couple to the RMAC rotor model shown in Fig. 8. The drivetrain model takes inputs for the desired speed (derived from the vehicle attitude/heave control) and rotor torque (taken from the aerodynamic model), and outputs the rotor speed. The actual rotor speed (along with the rotor hub motion) is used to model the aerodynamic forces and moments about the rotor hub, which are passed along to the vehicle dynamics model.

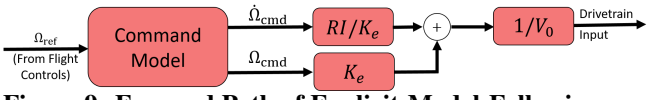

Figure 9: Forward Path of Explicit-Model-Following controller

Speed Control Architecture

The controller in Fig. 1 is divided into two parts, namely a low-frequency feedback controller (for the regulation of speed), and switching controller (to coordinate the switching in the converter). Naturally, the second component is only necessary when switching is actually modeled (only for the trapezoidal motor in this study), but the first component is needed for all machine types. The control architecture chosen for the speed control is explicit-model-following, the forward path of which is shown in Fig. 9. First, the reference signal is passed through a command model, which can be tuned based on handling qualities requirements (Refs. 5, 7, 8). The command model outputs a commanded speed, Ω_{cmd}, and an acceleration $\dot{\Omega}_{\text{cmd}}$. In the forward path, the commanded speed and acceleration are passed through a simplified inverse model, which predicts the required voltage input for the motor. The inverse model is taken from the simple DC motor (neglecting aerodynamic torque), without inductance, and used for all machine types.

$$\begin{aligned} \hat{G} &= \frac{V_0 K_e}{RIs + K_e^2} \\ u &= \frac{1}{K_e V_0}\left(RI\dot{\Omega}_{\text{cmd}} + K_e^2 \Omega_{\text{cmd}}\right) \end{aligned} \tag{9}$$

To account for deviations from this simplified model (due to inductance, aerodynamic torque, switching, etc.), feedback control is also included. For this application, a PI controller is used, with gains tuned using the simplest DC motor model. To ensure adequate frequency separation from the pitch/roll dynamics of the vehicle (tuned for a crossover frequency of 5 rad/s, Ref. 8), a crossover frequency of 25 rad/s for the rotor speed control loop is chosen. The zero location (the ratio of the integral grain to the proportional gain) is selected to be 1/5 of the crossover frequency (Ref. 30).

RESULTS

Isolated Rotor

A step command from 150 rad/s to 170 rad/s is commanded to each rotor model. Figures 10a and 10b show the response for each of the four machine types. Each of the motors have nearly identical speed responses, which is expected due to the small inductance and time constant of the motor. Delays associated with the motor inductance are negligible, as high-frequency commands (where the inductance will cause more phase delay) are filtered out by the command model. There is a small difference visible in the initial response of the trapezoidal motor, with brief lulls in the acceleration due to current/torque ripple as the commutating switches open and close.

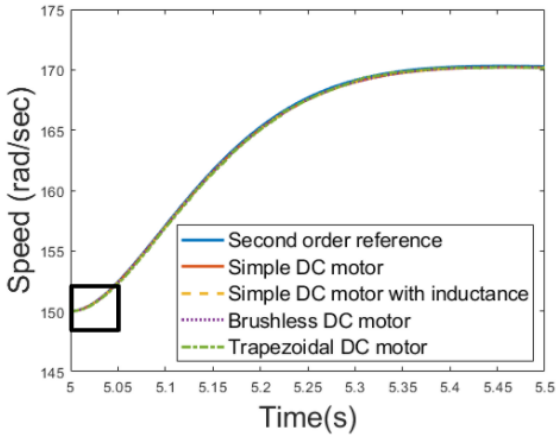

(a) First 500ms of the response

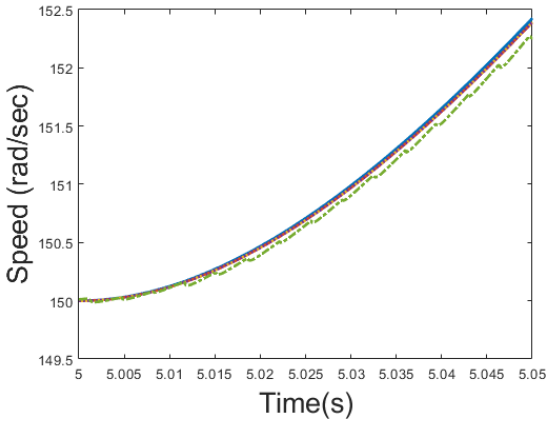

(b) First 50ms of the response

Figure 10: Second order speed command response.

While the dynamics of each of the machine configurations are nearly identical, the current draw varies significantly between the motor models, as shown in Fig. 11a. Of the three non-switching motors, it is clear that the simple DC motor requires the least current, topping out around 72A. The simple DC motor with inductance and the averaged BLDC motor require greater current during the step command, as the inductors become charged, drawing a peak of 78A, but is characteristically similar to the model that neglects inductance. The trapezoidal motor, on the other hand, is characterized by frequent drops to zero current, as the switching between phases occurs. For a brief moment, both of the switches in Fig. 6 are open, resulting in zero current.

The level of detail in the machine and converter model also impacts the motor torque. Figure 12a shows that the trapezoidal brushless motor model has the same switching behavior seen in the current, again caused by the transistor switching in the converter. Even without the switching, the inductance creates a small ripple torque, as seen in Figure 12b, though this is very small in magnitude compared to the switching torque ripple. This type of ripple will cause large periodic loading in the rotor shaft, which may cause fatigue.

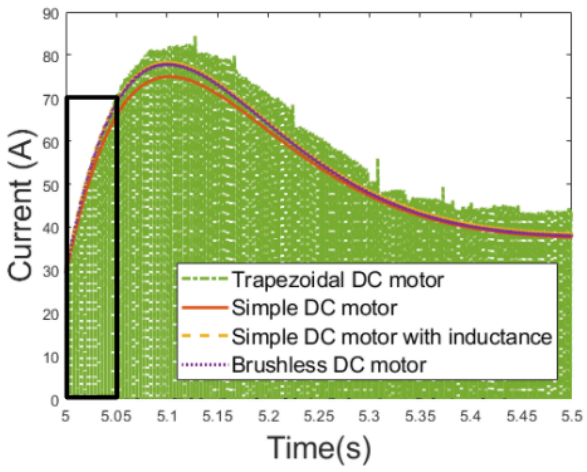

(a) First 500ms of the response

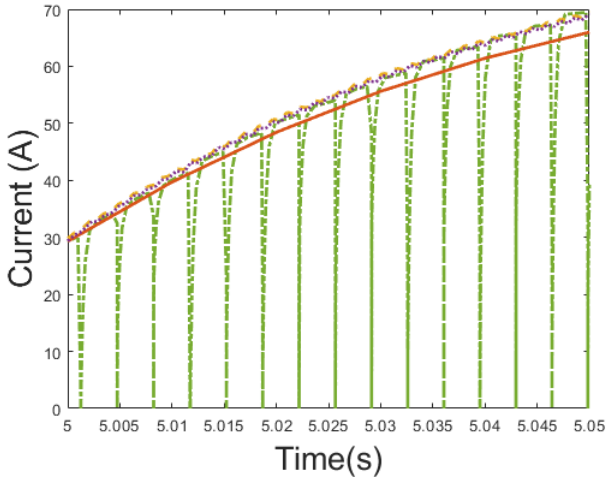

(b) First 50ms of the response

Figure 11: Motor current when a second order speed command is applied.

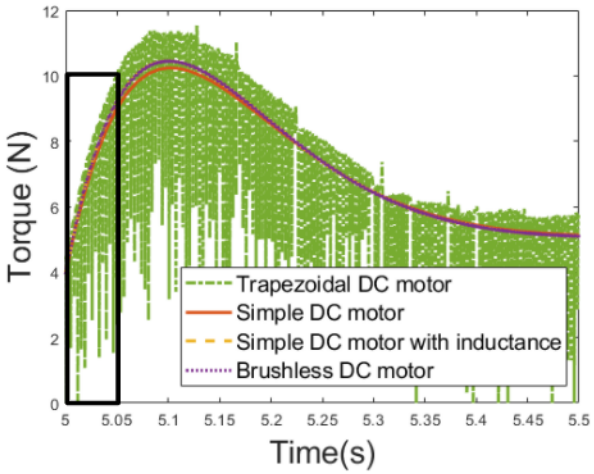

(a) First 500ms of the response

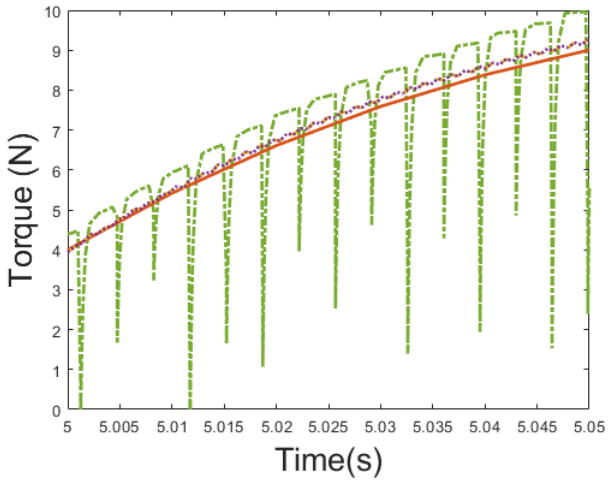

(b) First 50ms of the response

Figure 12: Motor torque when a second order speed command is applied.

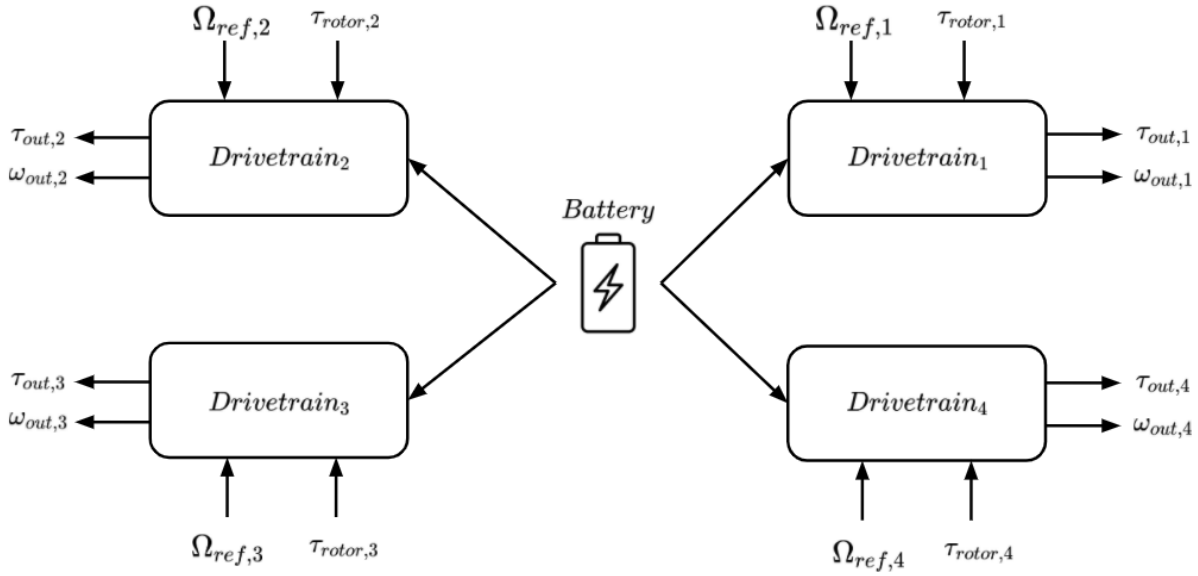

Figure 13: Multi-rotor aircraft model with centralized battery.

MULTI-ROTOR SYSTEM

Centralized Battery Architecture

To observe the loads of drivetrain architectures during maneuvering flight, the heave and pitch maneuvers are executed. Namely, a 5 m/s climb is commanded for 10 seconds (for a 50m climb) followed by a return to hover, and a 10 degree doublet is executed in pitch. First, a fully centralized battery architecture (Fig. 13), which provides power for all four motors, and one with a fully distributed battery (so that each motor has an independent power source). Because all of the motors had nearly identical behavior in terms of speed, the averaged BLDC motor is used in all of the simulations. Three power sources are used in this study. To match the conditions in Ref. 8, the second-order filter previously used is replaced with a first-order filter, tuned to meet ADS-33 handling qualities standards.

1. An ideal, 60V voltage source
2. A centralized battery at full charge (beginning of a mission)
3. A centralized battery at 30% charge (end of a mission)

Heave Command To examine the closed-loop behavior in heave, a 5 m/s climb rate is commanded to the vehicle and held for 10 seconds, so that the vehicle climbs 50m in total. The unfiltered command, along with the vehicle response is given by Fig. 14. The difference between the command and response is primarily due to the heave command model, which is first-order ($\tau = 4.6$ sec) by design. Figure 15 shows the corresponding rotor speed (all four motors receive identical commands in heave), and the tracking is nearly perfect for all configurations, though there is a very slight lag for both OCV batteries. Figure 16 shows the current drawn from the batteries during the heave maneuver, while Fig. 17 shows the battery voltage during the same. As the initial climb command is issued, the initial need to increase thrust (and thus rotor speed) produces an immediate spike in the current draw. As

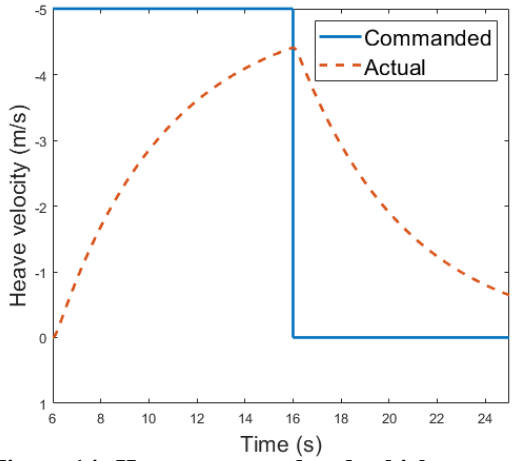

Figure 14: Heave command and vehicle response.

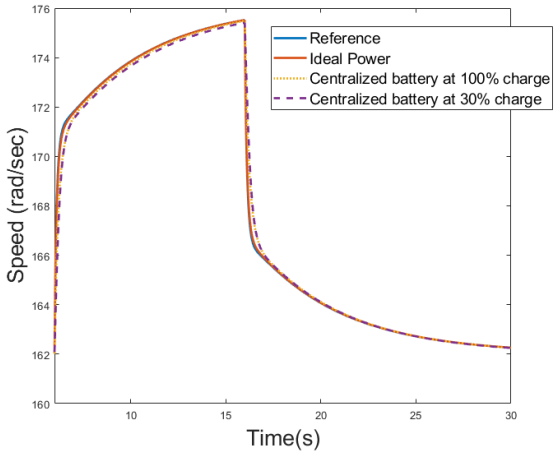

Figure 15: Speed response of multi-rotor system to heave command.

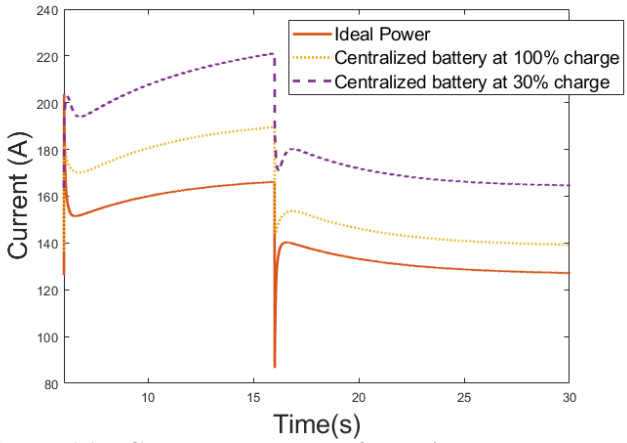

Figure 16: Current response of multi-rotor system to heave command.

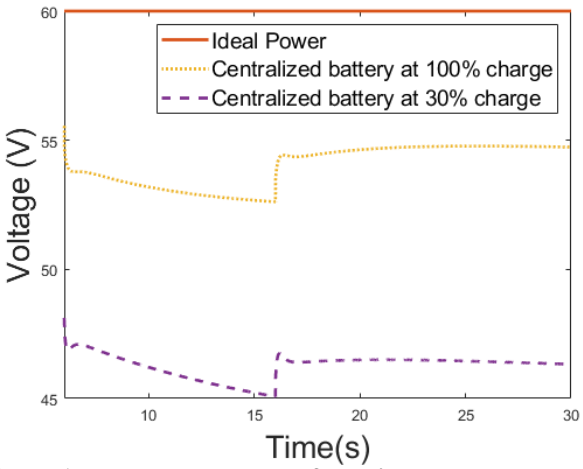

Figure 17: Voltage response of multi-rotor system to heave command.

the vehicle's climb rate increases, the additional downwash on the rotors increases the torque, leading to a smooth rise in the current drawn. When the climb command is terminated, the rotors slow down, producing a large negative spike in current, and as the aircraft returns to hover, the current and voltage approach their steady-state values. Generally speaking, the ideal voltage source drawn less current than the OCV batteries. This is due to the lower voltage delivered by the OCV batteries (represented by the resistors in Fig. 7) as current is drawn. The drop in voltage observed for the OCV batteries during the climb are also due to increased current demands; when the climb command is stopped, the voltage mostly recovers to its initial value. Naturally, the 30% charged battery has a lower overall voltage than the fully-charged one, so its current demands are even higher (the same power must be delivered to the motors in all three cases).

Pitch Command To examine the behavior in pitch, a 10 degree pitch doublet is commanded to the quadcopter, as shown in Fig. 18. The command model for pitch is a second-order transfer function ($\zeta = 0.7$, $\omega_n = 3.46$ rad/s). As discussed in (Ref. 8), the vehicle does not track the filtered command well, and the vehicle does not settle to 10 degrees before the doublet ends. The rotor speeds during the pitch doublet are shown in Figure 19. The front and rear rotors receive opposite commands, since they are on opposite sides of the pitch axis (Fig. 20). The current draw from the battery is shown in Figure 21. Unlike the heave command, the large spikes as the maneuver begins are not observed in the battery current, despite the large spike in the front rotors' current draw. This is because while the front rotors initially speed up (drawing more current), the rear rotors slow down (drawing less). Thus, the spikes in the battery current draw are small, and the corresponding changes in the voltage (Fig. 22) are similarly small. This behavior also applies to the roll and yaw axes. Therefore, when a centralized battery architecture is used, heave maneuvers at low charge represent the limiting case for battery current delivery.

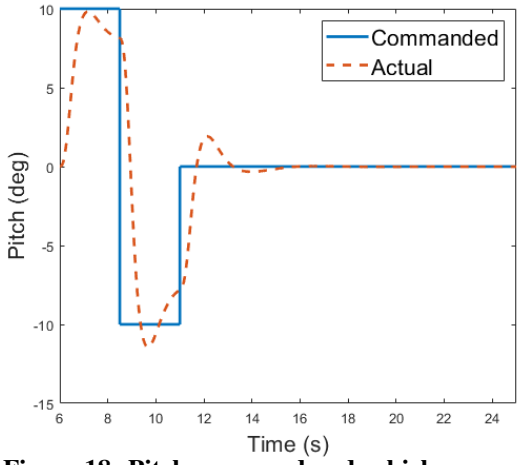

Figure 18: Pitch command and vehicle response.

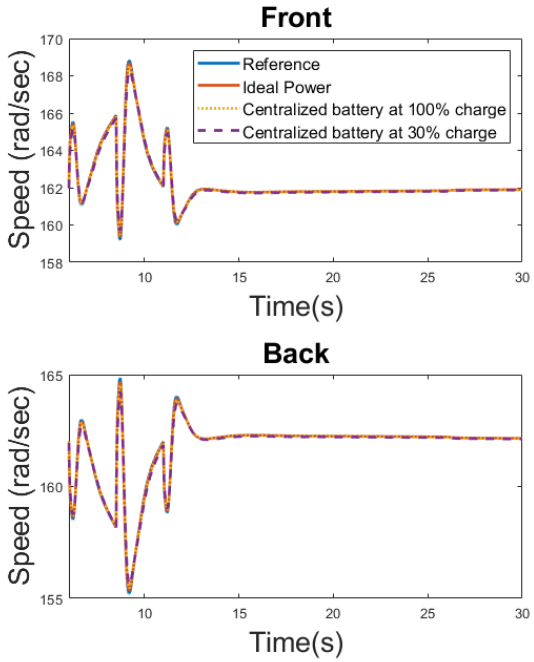

Figure 19: Speed response of multi-rotor system to pitch command.

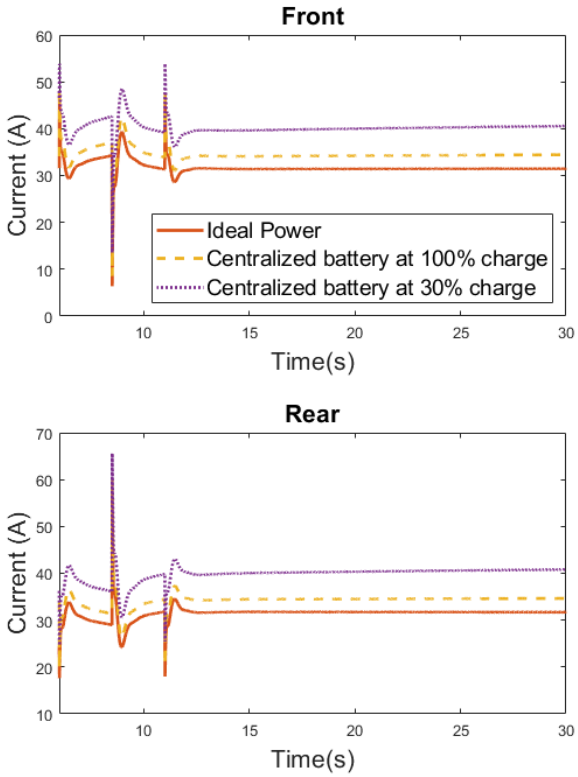

Figure 20: Current response of front and rear motors of multi-rotor system to pitch command.

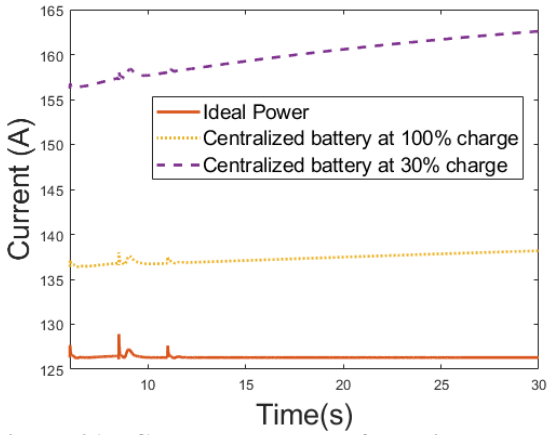

Figure 21: Current response of multi-rotor system battery to pitch command.

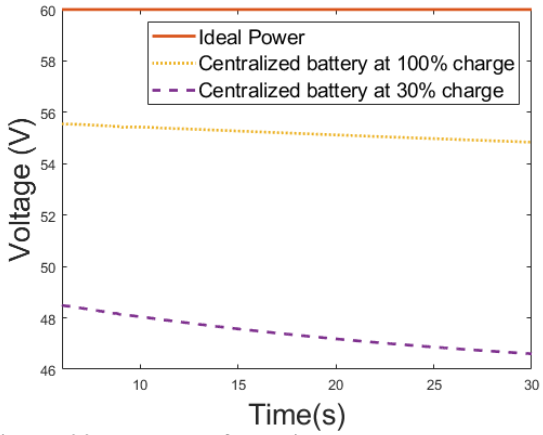

Figure 22: Voltage of multi-rotor system when pitch command is applied.

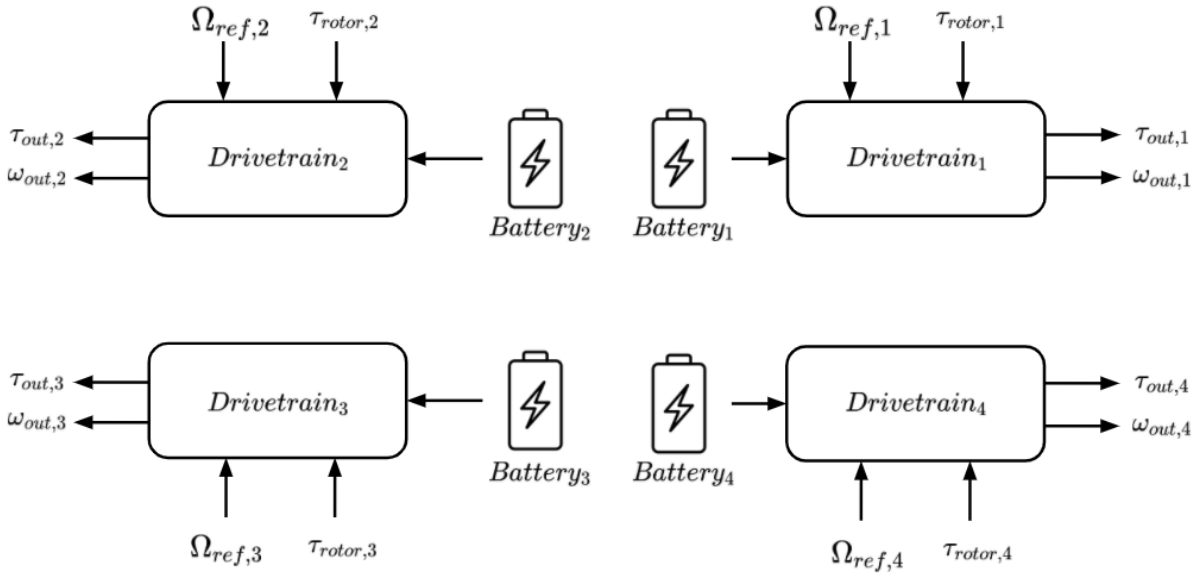

Figure 23: Multi-rotor aircraft model with individual batteries connected to each motor, creating a distributed architecture.

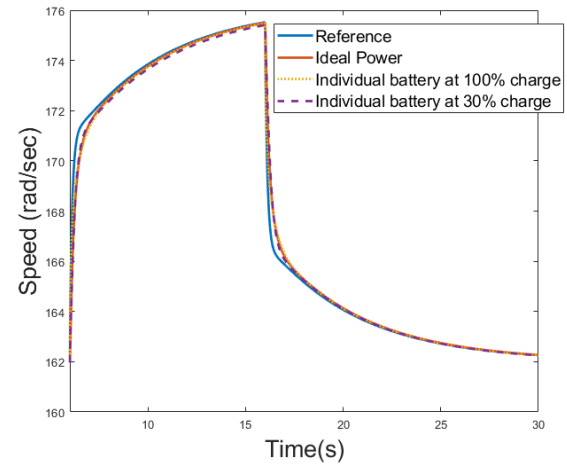

Figure 24: Speed response of multi-rotor system with individual batteries to heave command.

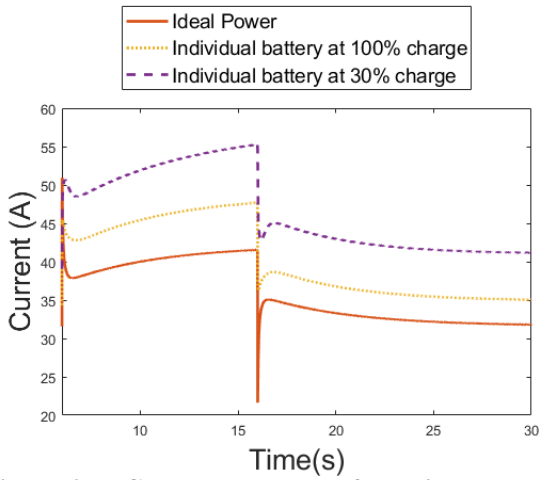

Figure 25: Current response of multi-rotor system with individual batteries to heave command.

Distributed Battery Architecture.

The distributed battery architecture is shown in Figure 23, where each of the motors in the drivetrain has its own power source. Each of the four batteries is one-fourth the size of the single battery pack that drives the centralized architecture. The same heave and pitch maneuvers used on the centralized battery architecture are applied to examine the demands on the powertrain.

Heave Command The heave command in Figure 14 is applied to the multi-rotor system with a distributed battery architecture. The speed response (shown in Fig. 24) is identical to that of the centralized battery, as might be expected, considering that heave commands load all four rotors identically. The current draw (Fig. 25) is exactly one-fourth (***or should be, once we fix the figure*** of the current observed for the centralized battery architecture (compare to Fig. 16), an intuitive result, since each battery is responsible for one fourth of the powertrain. Since the capacity of each individual battery is also one-fourth that of the centralized battery, the voltage behavior (Fig. 26) is identical to the centralized battery.

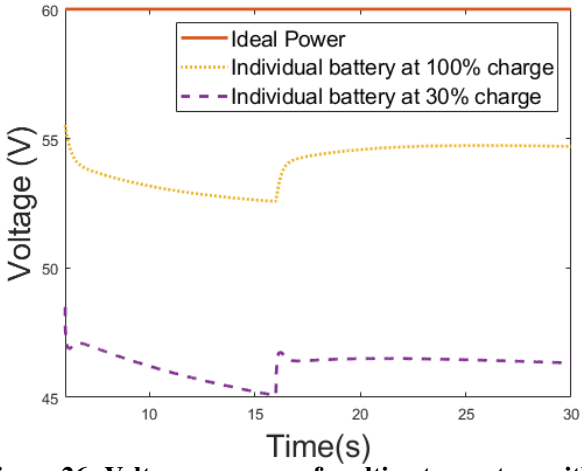

Figure 26: Voltage response of multi-rotor system with individual batteries to heave command.

Pitch Command The pitch command and vehicle response are shown in Figure 18. The rotor speeds during the pitch doublet are shown in Figure 27. The ability to track commanded velocities is identical to the centralized battery architecture (compare to Fig. 19). However, the current response (Fig. 28) is characteristically different. Because the front rotors' batteries are not connected to the rear rotors, the additional current drawn during a nose-up is not offset by the reduced current requirement of the rear rotors, and vice-versa. Thus, the current demands during pitch maneuvers will affect the battery sizing and cooling requirements. The batteries' voltage also changes during the doublet (Fig. 29), though not as dramatically as during the heave maneuver.

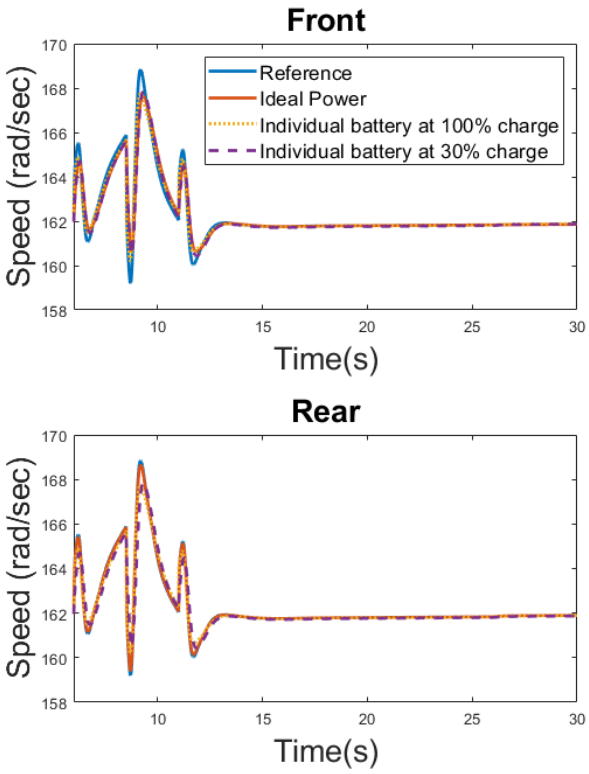

Figure 27: Speed response of multi-rotor system with individual batteries to pitch command.

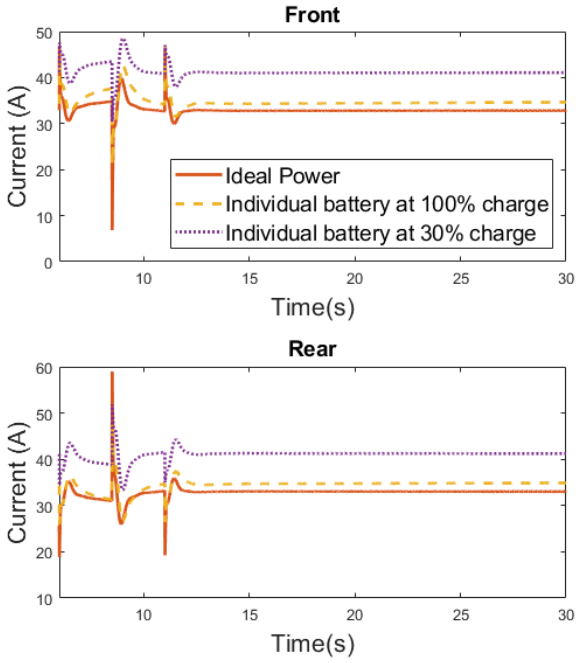

Figure 28: Current response of multi-rotor system with individual batteries to pitch command.

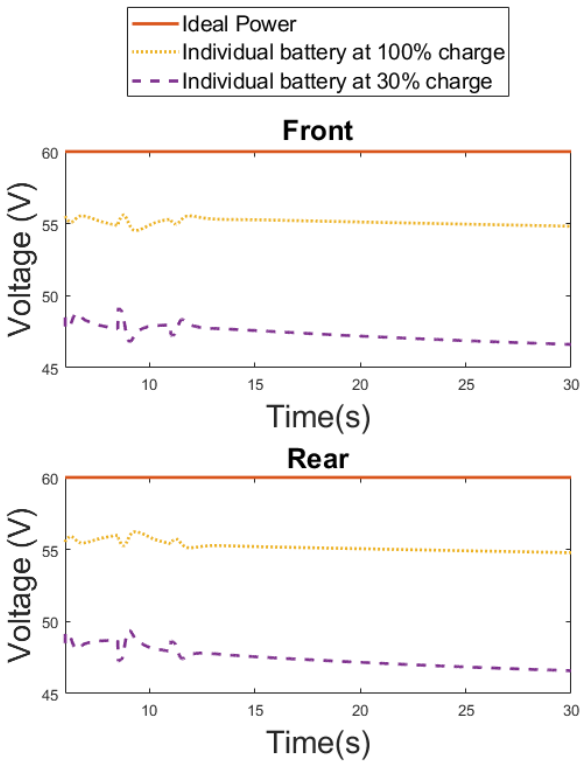

Figure 29: Voltage of multi-rotor system with individual batteries to pitch command.

Unbalanced battery charge Because the batteries in the distributed architecture are electrically decoupled from one another, it is plausible that, by the end of a flight, the batteries will have different states of charge. For example, as the rear rotors must spin faster (and consume more power) to maintain a nose-down pitch attitude in cruise, the rear batteries will discharge more than the front ones (assuming that the batteries are evenly divided between the rotors). To determine whether this might affect the tracking of speed commands, the same heave command is issued to a quadcopter whose front batteries are 40% charged and rear rotors are 30% charged.

The rotor speeds during the 50m climb are plotted in Fig. 30a. The speed of the front motors very slightly lag the speed of the back motors (Fig. 30b), though this will not result in any meaningful differences in the vehicle dynamics. Thus, it is clear that power delivery is not a limiting factor for the lithium polymer batteries used in this study, even when the charge is very low.

Figures 31 and 32 show the current and voltage in the front and back motors in aircraft. The back motors batteries are 6V higher than the front motors. As both of these motors must deliver the same power to the rotors during the climb, the current is greater for the rear batteries than the front.

CONCLUSION AND FUTURE WORKS

Several drivetrain models and configurations were simulated on a 1200lb quadcopter. While the motor model has little effect on the tracking performance to rotor speed commands

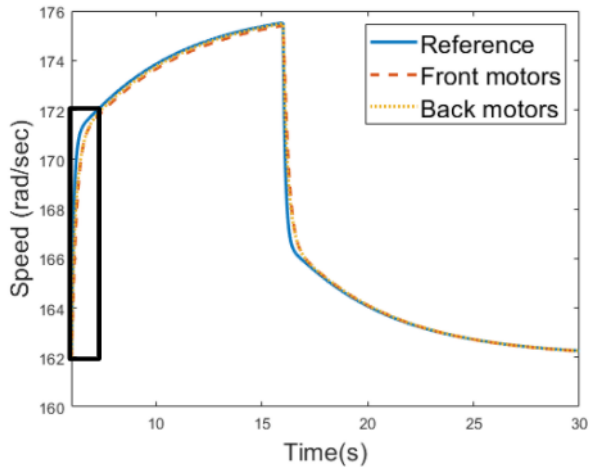

(a) Speed response of multi-rotor system to heave command with imbalanced batteries.

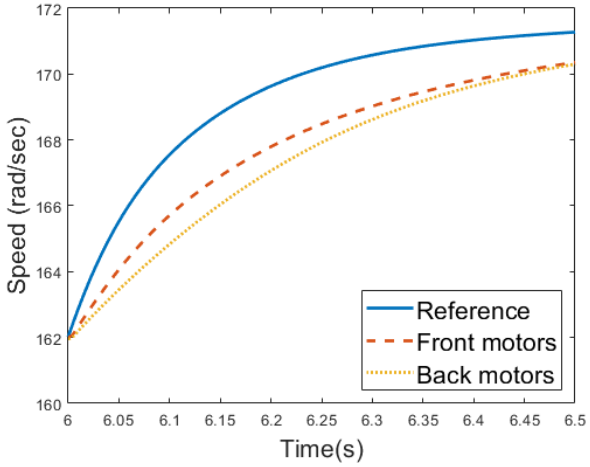

(b) Inset from 6 to 6.5 seconds.

Figure 30: Speed response of multi-rotor system to heave command with unbalanced batteries

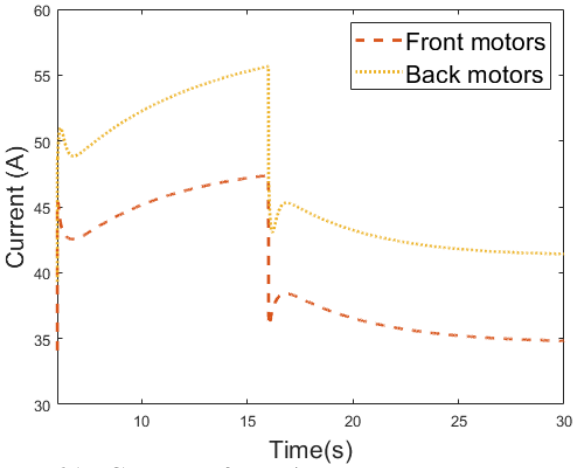

Figure 31: Current of multi-rotor system to heave command with unbalanced batteries

(and thus little effect on the flight dynamics), the torque ripple present due to the switching behavior can lead to faster degradation of components in the system, and the simplified

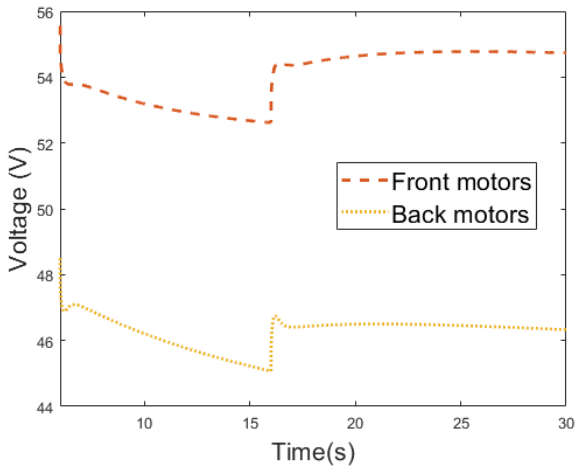

Figure 32: Voltage response of multi-rotor system to heave command with unbalanced batteries

models commonly used for flight dynamics are not adequate to capture this phenomenon.

The power source model has noticeable impact on the drivetrain performance. Relative to a constant voltage source, the OCV battery model predicts substantial changes in the battery source voltage and current, which is particularly apparent for low states of charge. The additional current drawn from the battery can lead to greater resistance losses and heat generation in the powertrain.

Finally, a fully-centralized battery architecture was compared to a fully-distributed architecture. Though both configurations were adequate in terms of rotor speed tracking, the centralized battery experienced very little variation in its load during pitch maneuvers, since accelerating rotors were always offset by decelerating rotors. In the distributed architecture, each battery must be sized based on the maximum current demanded during heave/pitch/roll/yaw maneuvers, while the centralized battery must only be sized for heave maneuvers.

ACKNOWLEDGMENTS

This work was supported in part by the National Aeronautics and Space Administration under award number 80NSSC19M0125 as part of the Center for High-Efficiency Electrical Technologies for Aircraft (CHEETA).

The first author is supported by the National Science Foundation Graduate Research Fellowship Program under Grant No. DGE 1744655 and the Chateaubriand Fellowship of the Office for Science & Technology of the Embassy of France in the United States.

The second author is supported by the Army/Navy/NASA Vertical Lift Research Center of Excellence (VLRCOE) Program, grant number W911W61120012 at RPI's Center for Mobility with Vertical Lift (MOVE), with Dr. Mahendra Bhagwat as Technical Monitor.

REFERENCES

1. NASA, "AAM Overview — NASA," https://www.nasa.gov/aeroresearch/aam/description/, 2020 (retrieved Nov 3, 2020).

2. Holden, J., and Goel, N., "Fast-Forwarding to a Future of On-Demand Urban Air Transportation," Available at: https://www.uber.com/elevate.pdf [Accessed 10 Oct. 2019], October 2016.

3. Malpica, C., and Withrow-Maser, S., "Handling Qualities Analysis of Blade Pitch and Rotor Speed Controlled eVTOL Quadrotor Concepts for Urban Air Mobility," VFS International Powered Lift Conference, San Jose, CA.

4. Withrow-Maser, S., Malpica, C., and Nagami, K., "Multirotor Configuration Trades Informed by Handling Qualitiies for Urban Air Mobility Application," 76th Annual VFS Forum, Virtual, October 6–8, 2020.

5. Niemiec, R., Gandhi, F., Lopez, M., and Tischler, M., "System Identification and Handling Qualities Predictions of an eVTOL Urban Air Mobility Aircraft Using Modern Flight Control Methods," 76th Annual VFS Forum.

6. Johnson, W., Silva, C., and Solis, E., "Concept Vehicles for VTOL Air Taxi Operations," AHS Technical Conference on Aeromechanics Design for Transformative Vertical Flight, San Francisco, CA, January 16–19, 2018.

7. Bahr, M., McKay, M., Niemiec, R., and Gandhi, F., "Handling Qualities Assessment of Large Variable-RPM Multi-Rotor Aircraft for Urban Air Mobility," 76th Annual VFS Forum.

8. Walter, A., McKay, M., Niemiec, R., Gandhi, F., and Ivler, C., "Hover Handling Qualities of Fixed-Pitch, Variable-RPM Quadcopters with Increasing Rotor Diameter," 76th Annual VFS Forum.

9. Pillay, P., and Krishnan, R., "Modeling, simulation, and analysis of permanent-magnet motor drives. I. The permanent-magnet synchronous motor drive," *IEEE Transactions on Industry Applications*, Vol. 25, (2), 1989, pp. 265–273.

10. Pillay, P., and Krishnan, R., "Modeling, simulation, and analysis of permanent-magnet motor drives. II. The brushless DC motor drive," *IEEE Transactions on Industry Applications*, Vol. 25, (2), 1989, pp. 274–279.

11. Perera, P. D. C., Blaabjerg, F., Pedersen, J. K., and Thogersen, P., "A sensorless, stable V/f control method for permanent-magnet synchronous motor drives," *IEEE Transactions on Industry Applications*, Vol. 39, (3), 2003, pp. 783–791. DOI: 10.1109/TIA.2003.810624

12. Schupbach, R. M., and Balda, J. C., "Comparing DC-DC converters for power management in hybrid electric vehicles," IEEE International Electric Machines and Drives Conference, 2003. IEMDC'03., Vol. 3, 2003.

13. Montesinos, D., Galceran, S., Blaabjerg, F., Sudria, A., and Gomis, O., "Sensorless control of PM synchronous motors and brushless DC motors - an overview and evaluation," 2005 European Conference on Power Electronics and Applications, 2005. DOI: 10.1109/EPE.2005.219492

14. Hayes, J., and Goodrazi, G. A., *Electric Powertain: Energy Systems, Power Electronics, and Drives for Hybrid, Electric, and Fuel Cell Vehicles*, Wiley, Hoboken, NJ, 2018, pp. 301–348.

15. Steigerwald, R. L., and Hopkins, D. C., "Characteristic Input Harmonics of DC-DC Converters and their Effect on Input Filter Design," *IEEE Transactions on Industrial Electronics and Control Instrumentation*, Vol. IECI-28, (2), 1981, pp. 73–82. DOI: 10.1109/TIECI.1981.351029

16. Xinxiang Yan, Seckold, A., and Patterson, D., "Development of a zero-voltage-transition bidirectional DC-DC converter for a brushless DC machine EV propulsion system," 2002 IEEE 33rd Annual IEEE Power Electronics Specialists Conference. Proceedings (Cat. No.02CH37289), Vol. 4, 2002. DOI: 10.1109/PSEC.2002.1023049

17. Liu, Y., Zhu, Z. Q., and Howe, D., "Commutation-Torque-Ripple Minimization in Direct-Torque-Controlled PM Brushless DC Drives," *IEEE Transactions on Industry Applications*, Vol. 43, (4), 2007, pp. 1012–1021. DOI: 10.1109/TIA.2007.900474

18. Ng, W., Patil, M., and Datta, A., "Hydrogen Fuel Cell and Battery Hybrid Architectures for Range Extension of Electric VTOL (eVTOL) Aircraft," 75th Annual VFS Forum, Philadelphia, PA, May 13–16, 2019.

19. Mills, B., and Datta, A., "Simulation and Characterization of Variable-Voltage Hybrid-Electric Powertrains," 76th Annual VFS Forum.

20. Ricci, M., Rahn, R., Myers, J., and Paden, B., "Electric Propulsion Component Sizing for Optimal Aircraft Configuration," 76th Annual VFS Forum.

21. Estima, J. O., and Marques Cardoso, A. J., "Performance analysis of a PMSM drive for hybrid electric vehicles," The XIX International Conference on Electrical Machines - ICEM 2010, 2010. DOI: 10.1109/ICELMACH.2010.5608285

22. Speed, R., and Wallace, A. K., "Remedial strategies for brushless DC drive failures," *IEEE Transactions on Industry Applications*, Vol. 26, (2), 1990, pp. 259–266. DOI: 10.1109/28.54251

23. Xia, C., Xiao, Y., Chen, W., and Shi, T., "Torque Ripple Reduction in Brushless DC Drives Based on Reference Current Optimization Using Integral Variable Structure Control," *IEEE Transactions on Industrial Electronics*, Vol. 61, (2), 2014, pp. 738–752. DOI: 10.1109/TIE.2013.2254093

24. Podlaski, M., Vanfretti, L., Nademi, H., and Chang, H., "UAV Dynamics and Electric Power System Modeling and Visualization using Modelica and FMI," 76th Annual VFS Forum.

25. "Hacker Q150-45-4 Series Datasheet," https://HackerMotorUSA.com, 2021.

26. Fritzson, P., *Modelica: Equation-Based, Object-Oriented Modelling of Physical Systems*, Springer International Publishing, Cham, 2020, pp. 45–96.

27. Dassault Systemes, "CATIA Systems Brushless DC Drives Library," https://www.3ds.com/fileadmin/PRODUCTS/CATIA/DYMOLA/PDF/3DS_2017_CAT_BrushlessDCDrives_Flyer_A4.pdf, October 2020.

28. Dassault Systemes, "CATIA Systems Battery Library," https://www.3ds.com/fileadmin/PRODUCTS/CATIA/DYMOLA/PDF/3DS_2015_CATIA_BTY_Battery__Flyer_A4_WEB.pdf, October 2020.

29. "FMI Standard," https://fmi-standard.org/, October 2019.

30. Tischler, M., Berger, T., Ivler, C., Mansur, M., Cheung, K., and Soong, J., *Practical Methods for Aircraft and Rotorcraft Flight Control Design: An Optimization-Based Approach*, AIAA Education Series, Reston, VA, 2017.